





## ORIGINAL ARTICLE

Special Section: Tribute to Rien van Genuchten, Recipient of the 2023 Wolf Prize for Agriculture

# Modeling sub-resolution porosity of a heterogeneous carbonate rock sample

William Godoy<sup>1</sup>  | Elizabeth M. Pontedeiro<sup>1,2</sup> | Rafael A. B. R. Barros<sup>3</sup> | Enno T. de Vries<sup>2,4</sup>  | Amir Raouf<sup>2</sup> | Martinus Th. van Genuchten<sup>2,5</sup>  | Paulo Couto<sup>1</sup> 

<sup>1</sup>Department of Civil Engineering, Federal University of Rio de Janeiro, Rio de Janeiro, Brazil

<sup>2</sup>Department of Earth Sciences, Utrecht University, Utrecht, The Netherlands

<sup>3</sup>Nanotechnology Engineering Program, Federal University of Rio de Janeiro, Rio de Janeiro, Brazil

<sup>4</sup>Hydrogeology Department, KWR Water Research Institute, Nieuwegein, The Netherlands

<sup>5</sup>Department of Nuclear Engineering, Federal University of Rio de Janeiro, Rio de Janeiro, Brazil

## Correspondence

William Godoy, Department of Civil Engineering, Federal University of Rio de Janeiro, UFRJ, Ilha do Fundão, RJ, Brazil.  
Email: [wmgodoy97@gmail.com](mailto:wmgodoy97@gmail.com)

Assigned to Associate Editor Jirka Simunek.

## Abstract

Accurately estimating the petrophysical properties of heterogeneous carbonate rocks across various scales poses significant challenges, particularly within the context of water and hydrocarbon reservoir studies. Digital rock analysis techniques, such as X-ray computed microtomography and synchrotron-light-based imaging, are increasingly employed to study the complex pore structure of carbonate rocks. However, several technical limitations remain, notably the need to balance the volume of interest with the maximum achievable resolution, which is influenced by geometric properties of the source–detector distance in each apparatus. Typically, higher resolutions necessitate smaller sample volumes, leading to a portion of the pore structure (the sub-resolution or unresolved porosity), that remain undetected. In this study, X-ray microtomography is used to infer the fluid flow properties of a carbonate rock sample having a substantial fraction of porosity below the imaging resolution. The existence of unresolved porosity is verified by comparisons with nuclear magnetic resonance (NMR) data. We introduce a methodology for modeling the sub-resolution pore structure within images by accounting for unresolved pore bodies and pore throats derived from a predetermined distribution of pore throat radii. The process identifies preferential pathways between visible pores using the shortest distance and establishes connections between these pores by allocating pore bodies and throats along these paths, while ensuring compatibility with the NMR measurements. Single-phase flow simulations are conducted on the full volume of a selected heterogeneous rock sample by using the developed pore network model. Results are then compared with petrophysical data obtained from laboratory measurements.

## 1 | INTRODUCTION

Reliable estimates of the petrophysical properties of heterogeneous carbonate rocks, crucial for water and hydrocarbon reservoir studies as well as CO<sub>2</sub> sequestration analyses, present significant challenges across various scales

**Abbreviations:**  $\mu$ CT, X-ray computed microtomography; MDF, maximum distance factor; NCC, number of closest connections; NCZ, number of closest zones; NMR, nuclear magnetic resonance; PNM, pore network model; PSD, pore size distribution; REV, representative elementary volume.

This is an open access article under the terms of the [Creative Commons Attribution-NonCommercial-NoDerivs](https://creativecommons.org/licenses/by-nc-nd/4.0/) License, which permits use and distribution in any medium, provided the original work is properly cited, the use is non-commercial and no modifications or adaptations are made.

© 2024 The Author(s). *Vadose Zone Journal* published by Wiley Periodicals LLC on behalf of Soil Science Society of America.

(Sun et al., 2017). Digital rock analysis techniques are now used extensively to decode the complex pore structures inherent of carbonate rocks. They typically involve X-ray computed microtomography ( $\mu$ CT) (Blunt, 2017; Bultreys et al., 2015; Godoy et al., 2019; Suhrer et al., 2020), focused ion beam scanning electron microscopy (Devarapalli et al., 2017; Dvorkin et al., 2011), and/or synchrotron-light based imaging (Ferreira et al., 2019; Pak et al., 2023). These studies aim to navigate the trade-off between the volume of interest (VOI) pertaining to the volumetric dimensions of a rock sample and the resolution, which is tied to the smallest visible structures within the rock images (Carrillo et al., 2022).

A persistent hurdle in these analyses is accurate estimation of sub-resolution porosity, also known as unresolved porosity (Archilla et al., 2016; Blunt, 2017; Lucas et al., 2020). This fraction of porosity, not detectable due to resolution limitations, plays a pivotal role in fluid flow studies of carbonate rocks. Carbonate rocks often exhibit multi-modal pore size distributions (PSDs), involving a wide range of pore throat sizes from nanometers to macropores spanning several centimeters in diameter (Drexler et al., 2022; Silveira et al., 2022). For typical core samples with diameters around 5 cm, the  $\mu$ CT resolution is confined to a few micrometers (Ferreira et al., 2023; Lima et al., 2022). Achieving higher resolutions necessitates either focusing on a smaller sample area (thus reducing the VOI) or physically segmenting the sample for multiple scanning processes (Drexler et al., 2022; Lima et al., 2022).

Two widespread modeling approaches are utilized to deduce the petrophysical properties from  $\mu$ CT imaging data. One approach involves direct fluid flow simulations within the segmented images by employing either lattice Boltzmann methods (McClure et al., 2021; Vogel et al., 2005) or recreating an equivalent pore system through finite element mesh techniques (Saxena et al., 2017). A second strategy introduces an intermediary step to simplify the pore geometry and topology, thereby facilitating the generation of an approximate network of pore bodies and pore throats for subsequent use in a pore network model (PNM) (Bultreys et al., 2016; Gostick et al., 2016; Raouf et al., 2013). PNM approaches offer the advantage of lower computational demands for conducting single- and multi-phase fluid flow simulations compared to other numerical methods, thus enabling the study of larger sample volumes (Blunt, 2017; Godoy et al., 2019) and circumventing the need to calculate petrophysical parameters not based on a representative elementary volume (REV) of the sample.

Despite the efficiency of PNMs for larger volumes, a balance must be reached between rapid computation and the accuracy of results since the entire pore system cannot be represented once a specific resolution threshold is chosen. To enhance the prediction of petrophysical parameters, an additional modeling step can be integrated during the pore network generation phase. Alves et al. (2021), for this pur-

### Core Ideas

- Using digital rock analysis, we generated and reconnected sub-resolution pores of a carbonate rock sample.
- A workflow is presented to allow the reconnection of detectable and sub-resolution pores.
- We compared simulated absolute permeabilities of different pore networks with laboratory measurements.
- Digital rocks generated with a pore network model can serve as a complementary tool for studying fluid flow patterns.

pose, introduced a method to link  $\mu$ CT attenuation values with sub-resolution porosity. Suhrer et al. (2020) similarly explored the relationship between resolved and unresolved porosity in studies with digitized plug scale samples having varying resolutions. In these studies, petrophysical contributed by the unresolved porosity regions were based on data from the resolved porosity before conducting lattice Boltzmann or finite element simulations. Bultreys et al. (2016) employed “micro-links” to reconnect sub-resolution areas with the resolved porosity, adding pore throats from the unresolved porosity regions to clusters within the defined macropore region. Jiang et al. (2013) adopted a different tactic by creating a stochastic network at the microscale that connects to the resolved porosity region through pore throats.

This study seeks to address sub-resolution porosity by introducing a novel approach inspired by the work of de Vries et al. (2017) and Bultreys et al. (2016). The approach is predicated on the formation of pore bodies and pore throats according to a predetermined PSD. Our proposal involves reconnecting sub-resolution pores with those across the entire plug volume, rather than limiting the scope to only a portion of the sample.

## 2 | MATERIALS AND METHODS

### 2.1 | Sample preparation

The methodology outlined in this study was applied to a carbonate rock sample sourced from the Sergipe-Alagoas Basin, located in northeastern Brazil. More specifically, the sample was obtained from the Morro do Chaves Formation in São Miguel dos Campos, being the geographical location of previous research conducted by Godoy et al. (2019). The selected sample, designated as 1–4, was extracted from a geologic layer known as Bed 2B (Figure 1), as identified in the work of Corbett and Borghi (2013).

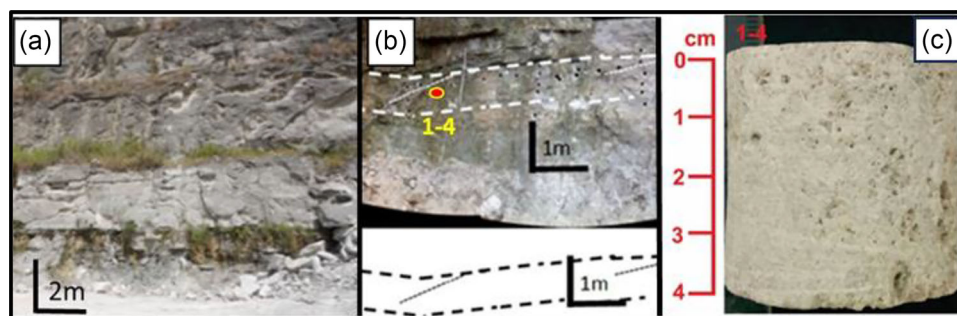


**FIGURE 1** (a) Image of the Morro do Chaves Formation in the Mina São Sebastião quarry in the city of São Miguel dos Campos, Brazil, (b) identification of layer (Bed 2B) from which samples 1–4 was taken (highlighted by a red point), and (c) a vertical view of the extracted sample (source: Modified from Godoy [2019]).

**TABLE 1** Parameters related to the acquisition and reconstruction of data of plug 1–4 as studied using the Bruker Skyscan 1173 X-ray computed microtomography ( $\mu$ CT) equipment.

Pixel size ( $\mu$ m)	Source voltage (kV)	Current ( $\mu$ A)	Ring artifact correction factor	Smoothing factor	Beam hardening correction (%)	Al/Cu filter (mm/mm)
9.97	130	61	5	4	15	0.5/0.5
18.53	130	61	13	5	20	0.5/0.5
24.95	130	61	4	3	20	0.5/0.5

The sample underwent a series of preparatory steps to ensure its suitability for further analysis. Initially, the top and bottom surfaces of the plug were flattened to create uniformity. The sample was subsequently subjected to a cleaning process for a period of 21 days using methanol and toluene. Following cleaning, the sample was dried in an oven at 60°C for a duration of 24 h. These preparatory procedures were conducted in accordance with methodologies previously adopted by Hoerlle et al. (2018). The final dimensions of the plug were measured to be approximately 35 mm in diameter and 40 mm in height.

## 2.2 | Imaging data analysis

For the pore structure analyses, we imaged the sample using the Bruker Skyscan 1173 equipment. The imaging process was carried out at three distinct resolutions to facilitate the identification of pore throat connections that may exist within sub-resolution regions. The multi-resolution approach allowed for a comprehensive examination of the sample's pore network. Following the acquisition of  $\mu$ CT images, a filtering step was implemented using the non-local means filter method described by Buades et al. (2005). Table 1 shows the primary parameters associated with the imaging data acquisition.

Measurements of the porosity and absolute permeability were conducted using the permeameter-porosimeter system DV-4000 (Weatherford Laboratories). The effective porosity was determined through helium (He) gas injection, while

the absolute permeability ( $K_{abs}$ ) was measured using nitrogen ( $N_2$ ), with Darcy's law applied to a steady flow regime. The helium porosity was found to be 0.147, and the  $N_2$   $K_{abs}$  was 33.19 mD.

Estimates of the effective porosity were also obtained using nuclear magnetic resonance (NMR) techniques (Blunt et al., 2013; Sullivan et al., 2007), which involved measuring the  $T_1$  and  $T_2$  relaxation times. This procedure was performed after the  $\mu$ CT imaging phase, with the sample being saturated in a saline solution. The solution consisted of 50,000 ppm sodium chloride (NaCl) and had a density of 1.039 g/cm<sup>3</sup> at a standard temperature of 25°C. Full saturation of the samples was achieved by applying an isostatic pressure of 2000 psi. To confirm the effectiveness of the saturation process, a saturation index was calculated at the end of the procedure. Table 2 outlines the primary parameters associated with the saturation process.

Table 3 shows a comparison between the porosity measurements obtained using the DV-4000 gas permeameter and those derived from the NMR techniques. Ensuring a close match between these two methods is crucial for accurately constructing the PSD curve, since discrepancies could lead to misinterpretations of the results. The PSD, based on NMR techniques and pore radii, was determined following the methodology of Luna et al. (2016) by converting  $T_2$  data into radii under the assumption that the pores are spherical, with a surface area factor ( $S$ ) set to 3.0.

The PSD and cumulative porosity curves for samples 1–4 are shown in Figure 2. The PSD curve indicates that a

TABLE 2 Parameters from the saturation index (SI) calculation.

Sample	Dried mass (g)	Saturated mass (g)	Brine density (g/cm <sup>3</sup> )	Pore volume (cm <sup>3</sup> )	SI (%)
1–4	82.21	87.43	1.039	5.26	95.51

TABLE 3 Porosity values obtained with permeameter and nuclear magnetic resonance (NMR) techniques.

Sample	Porosity NMR (%)	Porosity porosimeter (%)	Relative difference (%)
1–4	14.26	14.7	3.0

significant portion of the porosity is due to pores having radii <10  $\mu\text{m}$ , although the peak distribution occurs between 40 and 50  $\mu\text{m}$ . The sample had an average porosity typical of carbonate rocks (e.g., Mazzullo, 2004), but a relatively low permeability. The cumulative porosity curve further shows that approximately 20% of the porosity is contributed by pores with radii up to 10  $\mu\text{m}$ , an important aspect of this petrophysical property.

The  $N_2 K_{\text{abs}}$  value of samples 1–4 was determined to be 33.19 mD. This contrasts with other samples from the same Bed 2B (Godoy et al., 2019), which had far higher absolute permeability values (in the hundreds of mD) and a radius NMR peak distribution spanning hundreds of microns. This suggests that connectivity within samples 1–4 may have been influenced predominantly by the smaller pore throats associated with a secondary peak at approximately 0.1  $\mu\text{m}$  in Figure 2a compared with the main peak between radii of about 1  $\mu\text{m}$  and 500  $\mu\text{m}$ .

The segmentation process for the  $\mu\text{CT}$  images utilized a combination of NMR data and digital petrophysical rock data, employing various automated segmentation techniques (Kittler & Illingworth, 1986; Otsu, 1979). This approach enabled the selection of an optimal threshold value essential for the reconstruction of a calibrated three-dimensional

TABLE 4 Sub-resolution and detectable porosities from the reconstructed digital pore systems of samples 1–4.

Pixel size ( $\mu\text{m}$ )	Sub-resolution porosity (%)	Detectable porosity (%)	NMR porosity (%)
9.97	3.51	10.75	14.26
18.52	4.96	9.30	14.26
24.95	5.49	8.77	14.26

Abbreviation: NMR, nuclear magnetic resonance.

model, reflecting the porosity estimates derived from the  $\mu\text{CT}$  images. It is important to note that the spatial resolution of the structures is influenced not only by the pixel size of the detector but also by pixel blur, which is a result of the X-ray tube focal point dimensions. For the segmentation process, we used the Avizo 9.5 (Thermo Scientific) software (FEI), with threshold selection being a key step. Given that porosity estimation is based on the digital model generated from the  $\mu\text{CT}$  images, the pixel size is a critical factor in this process. Table 4 presents the porosity values obtained from both the NMR data and the reconstructed  $\mu\text{CT}$  images, according to the imaging resolution.

### 2.3 | Analysis of sub-resolution porosity

NMR data play a pivotal role in identifying the sizes of pore radii, including both pore bodies and pore throats that are not discernible or reconstructable due to the  $\mu\text{CT}$  resolution limitations. The absence of  $\mu\text{CT}$  data for the smaller pore structures can result in the creation of disconnected segments

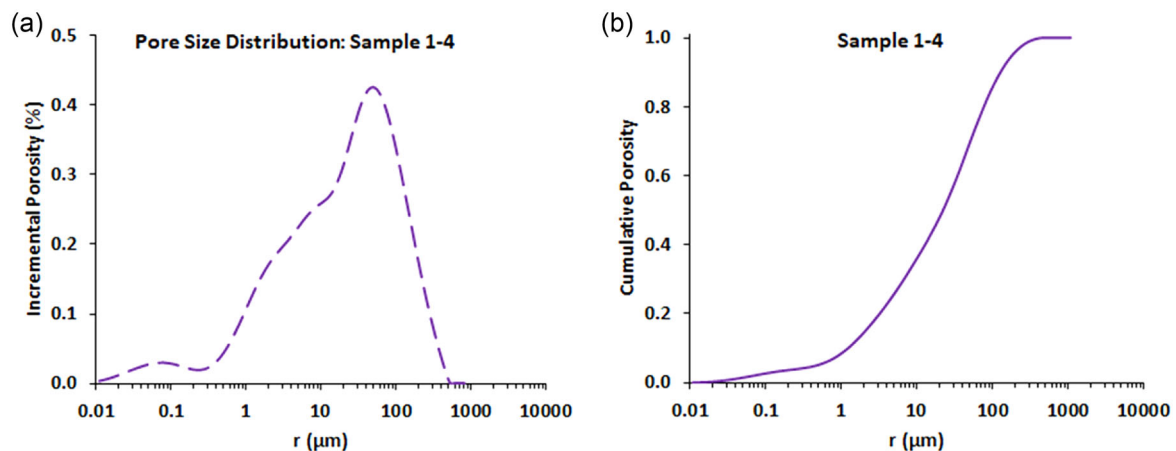


FIGURE 2 (a) Pore size distribution (PSD) curve obtained from the nuclear magnetic resonance (NMR) data, and (b) the cumulative porosity curve of samples 1–4 (source: Godoy [2019]).

within the pore networks. Pore network modeling facilitates the reconnection of these pore systems by generating sub-resolution pore structures.

The development of our PNM, based on visible porosity and the examination of input and output boundaries, adheres to the workflow outlined by Godoy et al. (2019). It is essential to recognize that different algorithms and workflows may yield varying outcomes, as demonstrated by Baychev et al. (2019). Our methodology for generating sub-resolution porosity and their connection with previously separated pore networks is based on the work of de Vries et al. (2017) and Bultreys et al. (2015, 2016), with some modifications in how the pores are connected.

The reconstruction of porous media from  $\mu$ CT image-derived networks using PNM techniques involves two main stages. Initially, the pore space is segmented into discrete elements, followed by measurements of the geometric properties for each element within the pore network, including radius, volume, length, and shape descriptors. These methodologies can be broadly categorized into two types: Topology-central methods, which focus on the separation of pore space based on the network topology, and morphology-central methods based on the central morphology of the pore space, as detailed by Bultreys et al. (2016). Drawing on this classification, de Vries et al. (2017) explored the complete pore structure of an aggregated soil by differentiating between the macropore and micropore domains. They developed algorithms to link pores on the aggregate's outer surface with adjacent macropores while randomly incorporating micropore aggregates distributed within the medium.

The core concept revolves around integrating pores and throats of dimensions smaller than those undetectable due to sample size limitations of the  $\mu$ CT system. This approach allows for the identification of undetectable porosity based on pixel size of the  $\mu$ CT images. Consequently, fluid flow through the entire pore system is facilitated by these smaller pores, which are interconnected with the larger pore systems, including vugs if present.

The primary challenge in constructing pore networks is to connect pore bodies without causing overlaps among multiple pore throats. To address this, we initiated connectivity studies using a guided random generation method within a confined volume. The method begins by identifying dissociated neighborhoods, or pore networks, which are interspersed with zones of indeterminate grayscale values in the  $\mu$ CT images, suggesting potential connectivity. We emphasize that these selected zones are likely candidates for sub-resolution pores, based on the grayscale intensity in the  $\mu$ CT images.

In the reconnection algorithm, pairs of pore bodies are designated: one from the neighborhood requiring connection and another one from the primary network. These pairs are then linked with the newly introduced sub-resolution pores. Prior to establishing connections, it is essential to identify

which networks within the model are disconnected but still are believed to be part of a larger, interconnected system. These networks, also referred to as neighborhoods, consist of a series of interconnected pores that form a self-contained system, isolated from the main pore network.

The distance between the separate neighborhoods and the main network often corresponds to the size of a pore throat, with the intervening space being an ill-defined region likely containing micropores that are undetected during imaging or overlooked during segmentation. To facilitate these connections, an auxiliary algorithm was developed to provide the necessary information, as illustrated in Figure 3. The algorithm employs a decision tree structure, where each node represents a pore body and each branch signifies a connection, grouping all pores into a single network. The method effectively eliminates connections between two or more pore bodies at the same hierarchical level, as well as connections involving a pore body common to the subsequent level.

Figure 3 outlines the algorithm's procedural steps:

1. An arbitrary pore is chosen as the "origin" or "reference." For instance, pore number 1 is selected, derived from the pore system's reconstruction based on the grayscale of the  $\mu$ CT images used for the PNM.
2. Pores connected to the origin (pore bodies 2 and 3) are identified, and their indices are recorded to prevent duplication. These pore bodies are generated in areas not recognized as pores post-segmentation due to their gray scale, yet are situated in lighter gray zones.
3. Each pore identified in the preceding step (i.e., pore bodies 2 and 3) is designated as the new origin.
4. Pores connected to any of the new origins (pore bodies 4 and 5) are identified and recorded.
5. Steps 3 and 4 are repeated until no new pores are generated, marking the completion of the network connectivity. At this stage, the newly generated and connected pore bodies link to pore bodies within the original main network (marked by number 6), which might already be connected to other pore bodies (as indicated by number 7). The algorithm concludes when no additional lighter grayscale regions are found, since these areas likely contain sub-resolution pores. The segmentation step defines these lighter gray regions, potentially housing sub-resolution pores, and the algorithm is confined to these areas.
6. All pores identified previously are classified as part of a neighborhood since they are interconnected. The process now restarts with a new arbitrary pore body not yet associated with any known neighborhood.
7. The algorithm concludes when there are no remaining ungrouped pores. In this scenario, pore bodies marked by numbers 6 and 7 could serve as new sources for generating connections with other neighborhoods, given the presence of regions whose gray scale may define areas likely to contain sub-resolution pores.

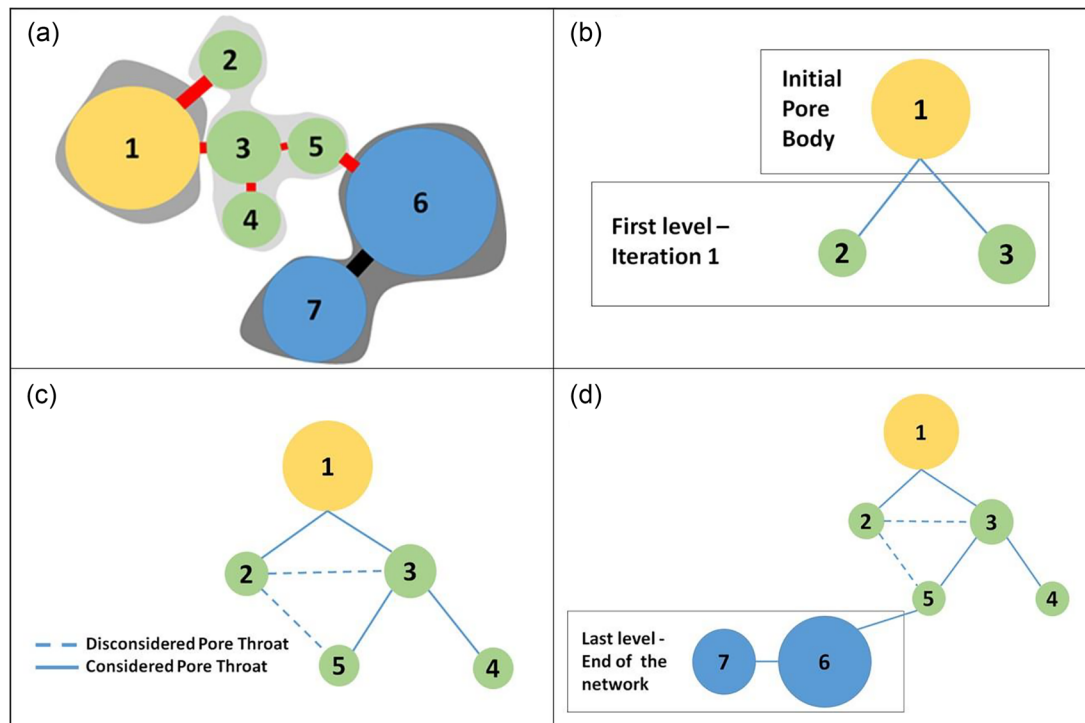


**FIGURE 3** Schematic of the adopted network generation: (a) real connections (pore throats in black) and generated connections (pore throats in red) in the pore network; (b) first iteration with definition of the first level (pore bodies generated and connected to previously existing networks); (c) second iteration in which redundant pore throats are discarded; and (d) last iteration, given the non-existence of connections with pore 7, and determination of the final network (*source*: Godoy [2019]).

As previously noted, the creation of connections between pore bodies does not involve pore throats that intersect with one another. Due to the significant computational demands required to verify intersections in large samples, we chose to generate and reconnect the pore systems while allowing for potential overlaps in the generated pore throats.

Given the resolutions used during the acquisition of  $\mu$ CT data for the selected samples, several assumptions were necessary:

1. The diameters of newly generated pores are inherently limited by the pixel size utilized during the  $\mu$ CT phase. If they were larger, they would have been detected during imaging.
2. The lower limit of the diameters is not easily determined geometrically. Nevertheless, the objective is to create a system that accurately represents the network's behavior rather than its precise structure. Therefore, the diameters must not be so small as to diminish their influence on subsequent simulations.
3. For instance, in our images with a pixel size of  $9.97 \mu\text{m}$ , the minimum and maximum pore size limits were established to be  $2.0 \mu\text{m}$  and  $9.1 \mu\text{m}$ , respectively. This range is considered to follow a uniform log-normal distribution due to the lack of a known distribution. The adopted limits

correspond to 20% and 98% of the smaller throat diameters for the given pixel size.

4. In images with a pixel size of approximately  $18.5 \mu\text{m}$ , the minimum and maximum pore sizes were estimated to be  $2.0 \mu\text{m}$  and  $18.2 \mu\text{m}$ , respectively. For a pixel size of  $24.95 \mu\text{m}$ , these limits were set at  $2.0 \mu\text{m}$  and  $24.5 \mu\text{m}$ .
5. The lower limits for both pore bodies and pore throats, regardless of the pixel size of the  $\mu$ CT images, were uniformly set at  $2.0 \mu\text{m}$ .
6. A log-normal distribution was chosen for the size distribution of the pores.

## 2.4 | Single-phase fluid flow numerical simulations

Numerical simulations to obtain the absolute permeability ( $K_{\text{abs}}$ ) were conducted following the methodology outlined by Godoy et al. (2019), who used a custom code partially based on the foundational work of Raouf et al. (2013). The simulations considered fluid flow along the  $z$ -axis, traversing from the top to the bottom of the sample. The  $K_{\text{abs}}$  calculations assumed laminar flow within the porous media, and employed Poiseuille's equation to determine the volumetric flow rate within each pore, that is,

$$Q_{ij} = \frac{\pi r_{ij}^4}{8\mu l_{ij}} (p_j - p_i) \quad (1)$$

where  $Q_{ij}$  represents the discharge through the pore throat between pore bodies  $i$  and  $j$ ,  $p_i$ , and  $p_j$  are the pressures at two adjacent pore bodies,  $r_{ij}$  is the radius of the pore throat,  $l_{ij}$  is the length of the throat, and  $\mu$  is the dynamic viscosity of the fluid (water).

For incompressible flow, the volume balance for each pore body  $i$  is calculated using:

$$\sum_{j=1}^{N_i} Q_{ij} = 0 \quad (i = 1, 2, 3, \dots, N_i) \quad (2)$$

where  $N_i$  is the coordination number of pore body  $i$ . Given a well-defined sample volume, the average fluid velocity within a pore,  $\bar{v}$ , can be determined as per Raouf et al. (2013):

$$\bar{v} = \frac{Q_{\text{tot}} L}{V_f} \quad (3)$$

where  $Q_{\text{tot}}$  is the total flow rate through the pore network, ascertainable at either the inlet or outlet as the sum of all flows,  $L$  represents the length of the pore network, and  $V_f$  is the total volume of the liquid phase within the pore network.

The sample's absolute permeability ( $K_{\text{abs}}$ ) is subsequently calculated using Darcy's equation:

$$K_{\text{abs}} = \frac{\nu Q_{\text{tot}} L}{A \Delta P} \quad (4)$$

where  $\mu$  is the fluid's viscosity (water),  $\Delta P$  is the pressure differential between the inlet and outlet (top and bottom of the sample, along the  $z$ -axis), and  $A$  is the cross-sectional area of the porous medium. For this study, we considered a pressure differential of  $5.0 \times 10^{-3}$  Pa between the upper and lower boundaries of the PNM along the vertical ( $z$ ) axis.

### 3 | RESULTS AND DISCUSSION

Our analysis of sub-resolution porosity was performed directly on the  $\mu$ CT images of sample plug 1–4. The images did not reveal any connections between the largest pore clusters within the system. Figure 4 illustrates the reconstructed pore network of samples 1–4, with  $\mu$ CT images captured at pixel sizes of 9.97, 18.53, and 24.95  $\mu\text{m}$  for images (a), (b), and (c), respectively.

Sub-resolution pores were generated using log-normal distribution given by

$$f(x | \mu, \sigma) = \frac{1}{x\sigma\sqrt{2\pi}} \exp\left\{-\frac{[\ln(x) - \mu]^2}{2\sigma^2}\right\} \quad (5)$$

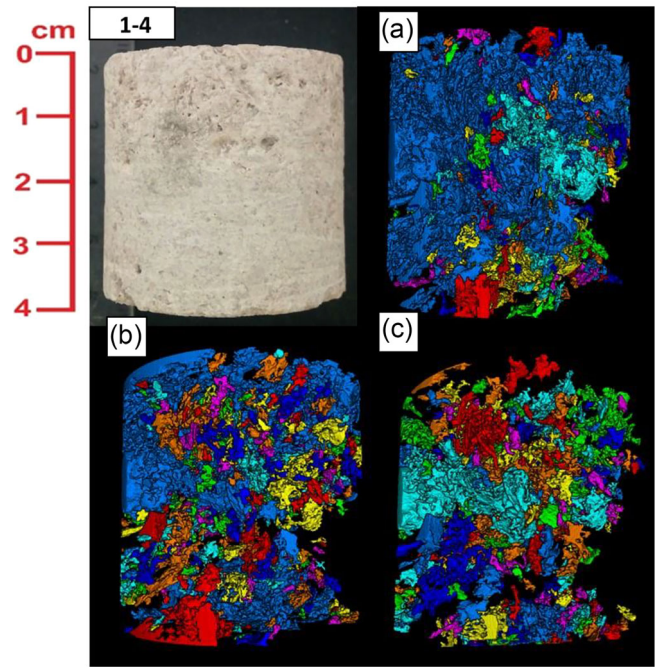


**FIGURE 4** Image of plug 1–4, and digital reconstructions of the porosity system based on X-ray computed microtomography ( $\mu$ CT) images having pixel sizes of (a) 24.95  $\mu\text{m}$ , (b) 18.16  $\mu\text{m}$ , and (c) 9.97  $\mu\text{m}$  (source: Godoy [2019]).

where  $x$  is the variable representing pore throat radii,  $\mu$  is the mean of the natural logarithm of  $x$ , and  $\sigma$  is the standard deviation of the natural logarithm of  $x$ . The parameters for the distribution were chosen as  $\mu = -4.71$  and  $\sigma = 0.0087$ , determined through the proposed reconnection algorithm. Figure 5 provides a plot of the generated pore throat radii.

The methodology allows one to control the number of sub-resolution pore bodies connected by adjusting three key parameters: the maximum distance factor (MDF), the number of closest zones (NCZ), and the number of closest connections (NCC). Of these, the parameter NCZ dictates the number of neighboring clusters to which each cluster can potentially connect, while NCC specifies the minimum number of connections that must exist between each cluster. These two parameters, in conjunction with the log-normal distribution characteristics, determine the dimensions of the pore bodies and throats to be generated, as well as their spatial placement within the overall network.

The MDF plays a crucial role in defining the maximum area within which sub-resolution pores can be generated and where connections between neighborhoods are possible. This parameter, which acts as a multiplier of the arithmetic mean of the pore throat lengths, effectively creates a sphere of influence. The NCZ specifies the number of neighboring regions that can be connected within the area defined by MDF, while the NCC determines the minimum number of connections that must exist between each neighborhood within the zone of interest.

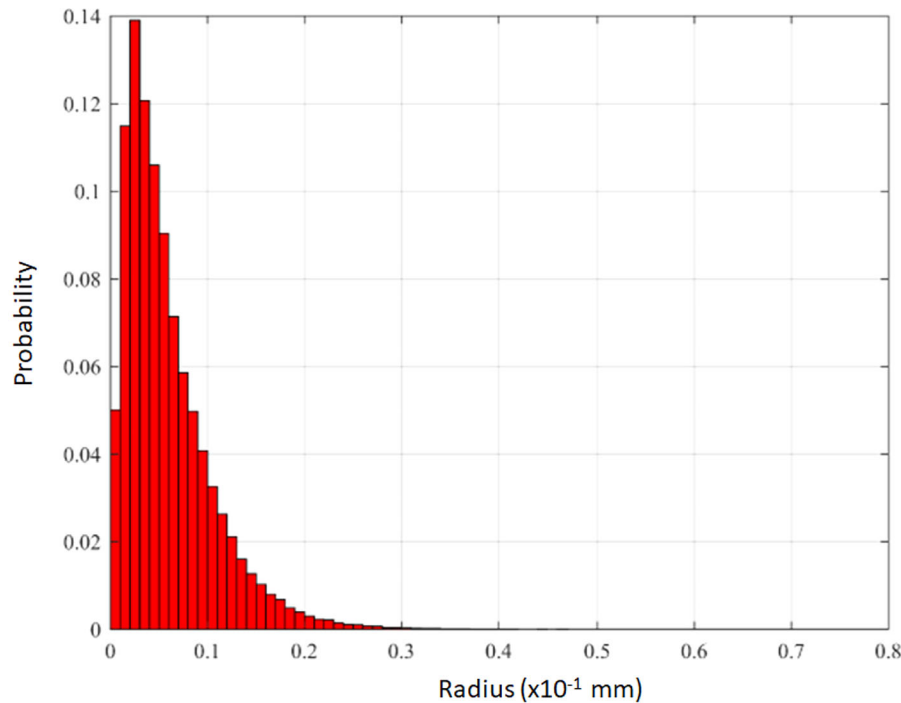


FIGURE 5 Plots of pore throat radii from the selected log-normal distribution to be used for the generation of sub-resolution pores.

The combined effects of the three parameters (MDF, NCZ, and NCC) significantly influence the estimates of the absolute permeability ( $K_{abs}$ ). A notable outcome of introducing new sub-resolution pores is their integration into previously isolated clusters, thus enabling the execution of numerical fluid flow simulations. This process facilitates connectivity within the original networks, which previously exhibited  $K_{abs}$  values of zero, despite the experimental  $K_{abs}$  being 33.19 mD.

We carried out an initial investigation about the effects of the MDF, NCZ, and NCC parameters on the PNM results using  $\mu$ CT images with a pixel size of 18.53  $\mu$ m. The input/output boundaries were adjusted to account for up to 2% along the flow ( $z$ ) axis, as per the methodology proposed by Godoy et al. (2019).  $K_{abs}$  estimates obtained from the numerical simulation of single-phase flow within the generated networks are present in Table 5. By varying each parameter individually, we aimed to discern their respective impacts on the simulation outcomes. Results indicate that NCZ had the most influence on the  $K_{abs}$  estimates, although the values were closely matched with all parameter combinations. Nonetheless, all estimated values were approximately one to two orders of magnitude lower than the experimentally measured value.

Given the unpredictability of the impact of the MDF, the NCZ, and the NCC parameters, they were initially chosen based on fundamental assumptions following preliminary simulations. These assumptions were as follows:

1. Geometric means were used for determining the dimensions of pore throats connected to the input/output bound-

TABLE 5 Pore network model (PNM) generated  $K_{abs}$  estimates using 18.53  $\mu$ m pixel size X-ray computed microtomography ( $\mu$ CT) images of samples 1–4 considering 2% of the flow domain for the input/output boundaries and using geometric averages when generating the pore throats.

Sample 1–4 PNM	Parameters			Estimated $K_{abs}$ mD
	MDF	NCZ	NCC	
Case 1	8	3	3	0.395
Case 2	8	3	4	0.445
Case 3	8	4	3	0.605
Case 4	9	3	3	0.576
Case 5	9	4	3	0.407

Abbreviations: MDF, maximum distance factor; NCC, number of closest connections; NCZ, number of closest zones.

- aries, which accounted for 2% of the network's dimension along the  $z$ -axis as noted previously.
2. The foundational pore network model was constructed using  $\mu$ CT images with a pixel size of 18.53  $\mu$ m. We anticipated that generating sub-resolution pores, establishing connections between neighborhoods, and conducting subsequent simulations to calculate the absolute permeability would be significantly more resource-intensive if the PNM was based on a much smaller pixel size of 9.97  $\mu$ m.
3. The initial value for MDF was set to eight times the arithmetic mean of the pore throat lengths. This decision was made under the premise that lower values would not facilitate sufficient connectivity to yield  $K_{abs}$  estimates that



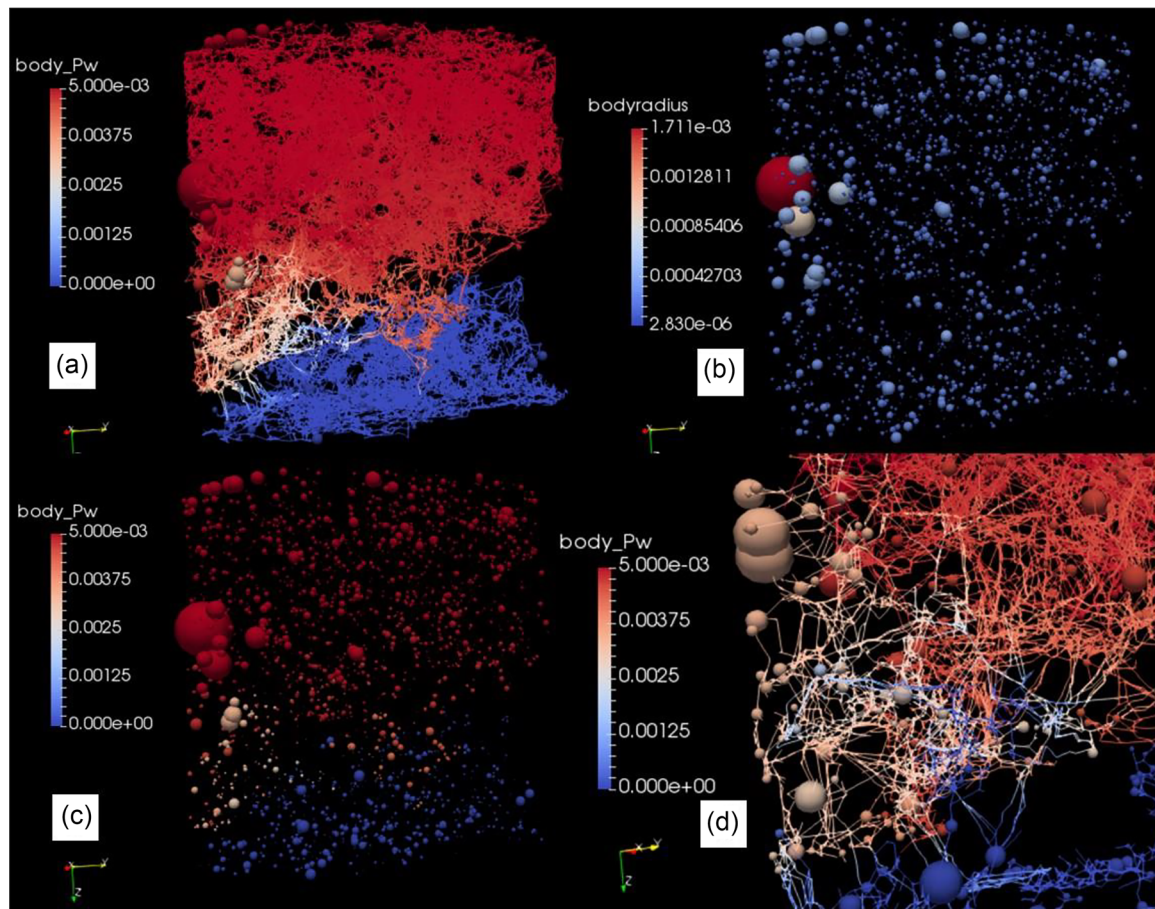


**FIGURE 6** (a) Results of the pressure field based on a pixel size of the X-ray computed microtomography ( $\mu$ CT) derived pore network model (PNM) image of  $18.53\ \mu\text{m}$  for Case 3, (b) pore body radii, (c) pore body pressures, showing in lighter colors the connected region, and (d) a zoom of this region. Pressure scales are measured in Pa, spatial dimensions measured in m (*source*: Godoy [2019]).

would closely align with the experimental value for our sample.

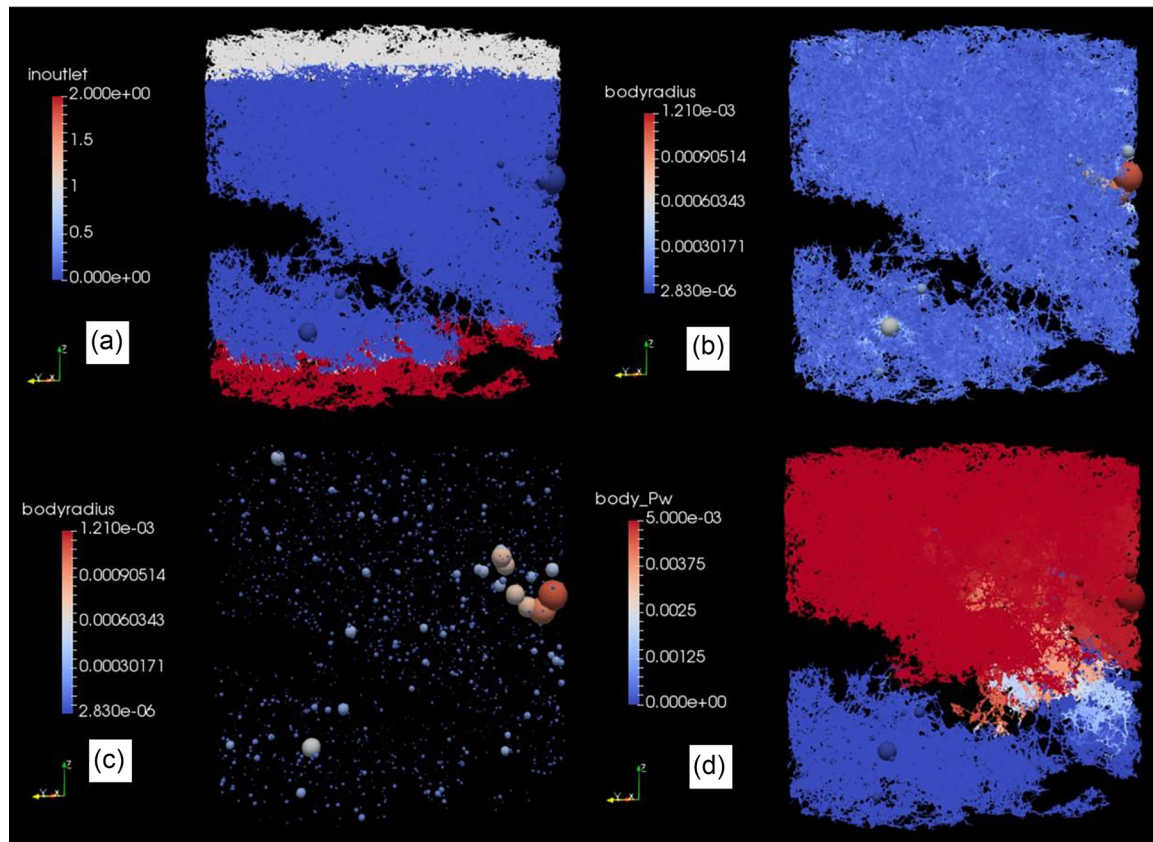
4. Values of 3 were selected for both NCZ and NCC to ensure a sufficient number of connections to enable fluid flow simulations and obtaining  $K_{\text{abs}}$  estimates. This initial setup hence envisioned three neighborhoods, each with three connections.
5. The initial baseline condition for evaluation was established with the reconstructed PNM having MDF, NCZ, and NCC values set to 8, 3, and 3, respectively.
6.  $K_{\text{abs}}$  values derived from the PNM could then be benchmarked against the experimental value obtained for this sample, which was 33.19 mD.

Figure 6 illustrates the results of numerical simulations focusing on the convergence of the pressure field for Case 3, as detail in Table 6. The radii of the pore bodies were significantly smaller than those derived directly from the PNM using images with a pixel size of  $18.53\ \mu\text{m}$ . Specifically, the directly measured smallest radii were  $9.265\ \mu\text{m}$ , while after the generation and reconnection of sub-resolution pores, the smallest radii were reduced to  $2.830\ \mu\text{m}$ , as shown in Figure 6b.

**TABLE 6**  $K_{\text{abs}}$  estimates based on pore network models (PNMs) generated from  $18.53\ \mu\text{m}$  pixel size X-ray computed microtomography ( $\mu$ CT) images for samples 1–4 considering geometric average for pore throats generated for Case 3 using different input/output boundaries.

Sample 1–4 $18.53\ \mu\text{m}$ (PNM)	Input/output boundaries (%)	$K_{\text{abs}}$ numerical simulation (mD)
	2	0.605
Case 3	10	3.85
	20	4.37

Table 7 provides similar estimates of  $K_{\text{abs}}$  using PNMs developed now from images with a pixel size of  $9.97\ \mu\text{m}$  and incorporating input/output boundaries set at 10% as per the methodology of Godoy et al. (2019). The pore systems were configured using parameters of values of 9, 4, and 3 for MDF, NCZ, and NCC, respectively.  $K_{\text{abs}}$  values were calculated for various averages (harmonic, geometric, and arithmetic) of the pore throat radii. Results show that the PNMs created with a higher resolution and input/output boundaries defined as 10% of the plug in the flow direction sections aligned more closely with the experimental value of 33.19 mD, despite all being



**FIGURE 7** Results of the pressure field based on a pixel size of the X-ray computed microtomography ( $\mu$ CT) derived pore network model (PNM) image of  $9.97 \mu\text{m}$  for Case 3, (b) pore body radii, (c) pore body pressures, showing in lighter colors the connected region, and (d) a zoom of this region. Pressure scales are measured in Pa, spatial dimensions measured in m (*source*: Godoy [2019]).

**TABLE 7**  $K_{\text{abs}}$  estimates based on pore network models (PNMs) generated using a pixel size of  $9.97 \mu\text{m}$  in the X-ray computed microtomography ( $\mu$ CT) images for samples 1–4, considering 10% of input/output boundaries and three ways of averaging the pore throat radii.

Sample 1–4 pore throats	Estimated numerical absolute permeability (mD)
Harmonic average	15.68
Geometric average	31.85
Arithmetic average	51.20

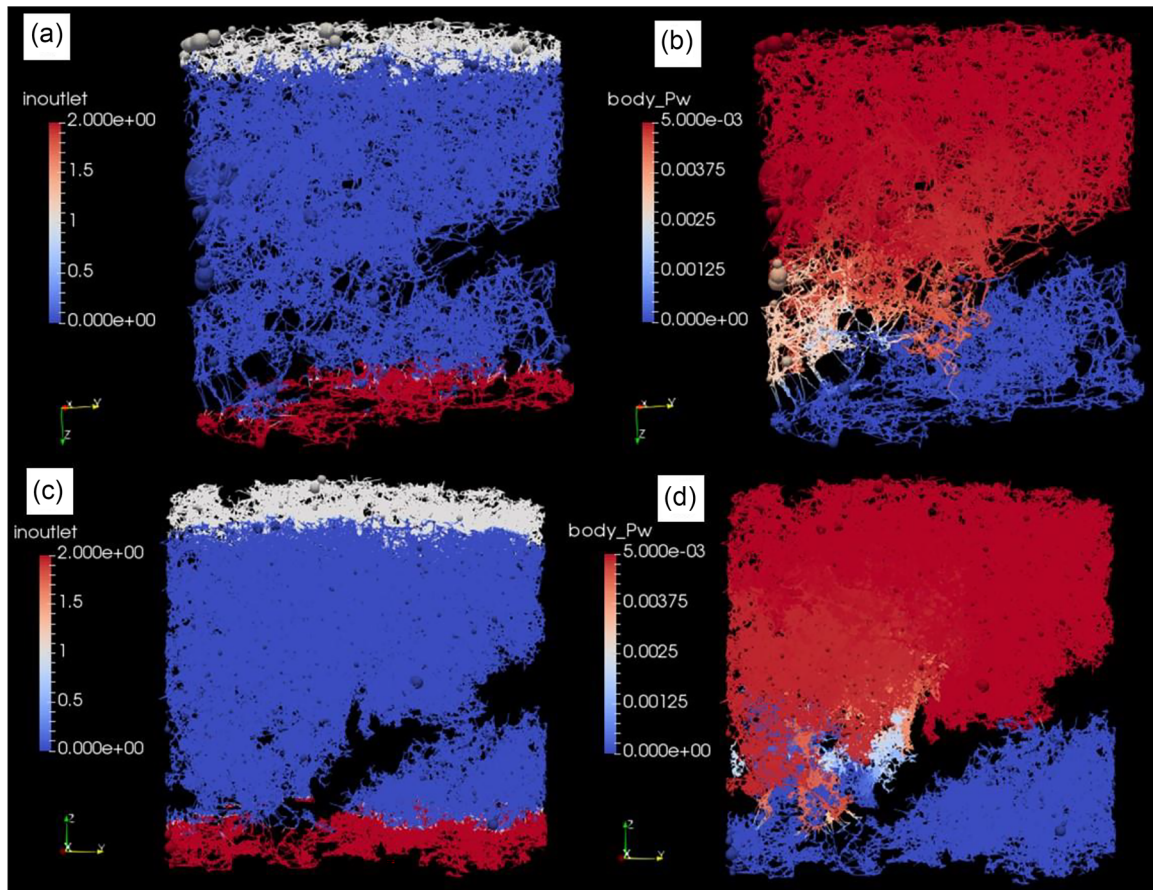
within the same order of magnitude. Notice that the PNM network using geometric means for the pore throats radii yielded a  $K_{\text{abs}}$  value most closely matching the reference value.

Figure 7 presents PNM outcomes derived from  $\mu$ CT images with a pixel size of  $9.97 \mu\text{m}$ , employing geometric means for the pore throats, 10% input/output boundaries, and MDF, NCZ, and NCC values of 9, 4, and 3, respectively. A numerically imposed pressure differential of  $5.0 \times 10^{-3}$  Pa was again applied. As previously discussed, the sub-resolution porosity was estimated from a log-normal distribution of the sub-resolution pore throats (Equation 5 with  $\mu = 4.71 \mu\text{m}$  and

$\sigma = 0.0087 \mu\text{m}$ ), reflecting a similar distribution pattern for macro-throats observed in the sample network.

Similarly, as for the PNMs generated with  $\mu$ CT images having pixel sizes equal to  $18.53 \mu\text{m}$  and  $24.95 \mu\text{m}$ , several assumptions were made regarding the insertion and reconnection of sub-resolution pores for the pore networks generated with a lower resolution. For networks obtained with  $\mu$ CT images having a pixel size of  $18.53 \mu\text{m}$ , numerically estimated  $K_{\text{abs}}$  values were consistently one or two orders of magnitude below the experimentally obtained reference value, even after the addition of sub-resolution pores. This discrepancy occurred regardless of the method used to define the pore throats (arithmetic, geometric, or harmonic), the specified input/output boundaries (2%, 10%, or 20%), and the values of MDF, NCZ, and NCC. Conversely, networks obtained with  $\mu$ CT images using a pixel size of  $24.95 \mu\text{m}$  did not show any connectivity between the neighborhoods when using the same parameters for the pore network and subsequent reconnections.

A significant advantage of our methodology for generating and reconnecting sub-resolution porosity is that the algorithm seeks connections within topological proximity between already existing pore bodies and pore throats and



**FIGURE 8** Pore network model (PNMs) of samples 1–4 based on 18.53  $\mu\text{m}$  (a) and 9.97  $\mu\text{m}$  (c) pixel size X-ray computed microtomography ( $\mu\text{CT}$ ) images assuming 10% input/output boundaries, and the pressure fields for those two PNMs (b and d, respectively). Pressure scales are measured in Pa (*source*: Godoy [2019]).

the newly generated sub-resolution pores. For comparison, Figure 8 presents the results of the pressure fields for the PNMs obtained with different resolutions. Notice that the generated sub-resolution pores facilitated the reconnection of neighborhoods in the vicinity of the same region as before (as shown in Figure 8b,d). The methodology minimizes the generation of new pores in regions initially not considered candidates for receiving new pores, particularly considering the gray scale of the  $\mu\text{CT}$  images, which suggests the absence of such pores.

Although the results are promising, further potential improvements to our methodology may include:

1. identifying specific regions for the insertion and connection of sub-resolution pore bodies and pore throats. This process could leverage the grayscale of the  $\mu\text{CT}$  images in selected areas with a high likelihood of containing sub-resolution porosity;
2. implementing multi-scale imaging techniques to examine certain regions with higher resolution images. This approach would increase confidence in identifying sub-porosity regions by assigning weights to areas most likely

to contain sub-resolution porosity, as suggested by Ruspini et al. (2021);

3. correlating the NMR derived pore size distribution with the distribution curve used during script execution. This correlation would help in fine-tuning the parameters used in the PNM model;
4. exploring additional experimental methods to calibrate the pore throat size distribution curves. This could involve utilizing data from mercury injection capillary pressure (MICP) techniques or acquiring  $\mu\text{CT}$  images of specific areas at higher resolutions to achieve more accurate pore system representations.

## 4 | CONCLUSIONS

Our investigation combined both experimental and numerical analyses of a carbonate rock sample from a Brazilian basin. Through a combination of direct laboratory measurements and  $\mu\text{CT}$ -based imaging techniques, we explored the rock matrix composition and digitally reconstructed pore systems. This comprehensive approach shed light on the matrix

and macropore fluid flow processes within a naturally heterogeneous rock sample. By employing PNM-based numerical simulations, we were able to estimate the absolute permeability of the entire plug, which aligned well with the measured REV.

The experimental findings played a crucial role in establishing significant correlations across the entire plug, primarily to gather accurate information about the pore structure necessary for the modeling phase. Higher resolution  $\mu$ CT images yielded the most accurate results for permeability, closely matching the experimental data for the entire plug. To develop more realistic pore systems for this carbonate rock sample, we incorporated additional experimental techniques, such as NMR to confirm prevailing pore distributions and refine the segmentation process for further PNM studies, particularly under multiphase flow conditions.

Our sub-resolution porosity investigations demonstrated a strong correlation between the numerical  $K_{\text{abs}}$  results and the laboratory measurement, following the selection of pore connection parameters. We emphasize that our efforts were intentionally directed toward establishing a viable digital workflow for generating and reconstructing sub-resolution porosity. This strategy was supported by physical data on PSD obtained using NMR, albeit without conducting further flow tests to assess potential impacts on pore predictions and associated fluid flow behavior. Future studies will focus on (a) enhancing the methodology for pore generation and reconnection in targeted sample regions; (b) achieving finer control of the PSDs through the use of NMR and MICP data for calibrating the curves generating pore bodies and throats; and (c) exploring the use of data from two-phase flow simulations for more accurate calibration of the generated networks. These avenues of research will be pursued in a broader study dedicated to sub-resolution porosity.

## AUTHOR CONTRIBUTIONS

**William Godoy:** Conceptualization; investigation; methodology; software; validation; writing—original draft. **Elizabeth M. Pontedeiro:** Investigation; methodology; supervision; validation; writing—review and editing. **Rafael A. B. R. Barros:** Conceptualization; methodology; software; writing—review and editing. **Enno T. de Vries:** Methodology; software; writing—review and editing. **Amir Raouf:** Investigation; software; supervision; writing—review and editing. **Martinius Th. van Genuchten:** Conceptualization; investigation; supervision; writing—review and editing. **Paulo Couto:** Investigation; supervision; writing—review and editing.

## ACKNOWLEDGMENTS

The authors would like to thank the Federal University of Rio de Janeiro (UFRJ) in Brazil and the Utrecht University in Utrecht, The Netherlands, for supporting this research. We thank Prof. Ricardo Tadeu from UFRJ (LIN) for providing the

X-ray computed microtomography images with different resolutions. We would also like to thank Prof. Leonardo Borghi from UFRJ (LAGESED) for the sample selection. The authors also like to thank William Godoy and UFRJ (COPPE) for the permission to use the images.

## CONFLICT OF INTEREST STATEMENT

The authors declare no conflicts of interest.

## ORCID

William Godoy  <https://orcid.org/0000-0003-1879-9386>

Enno T. de Vries  <https://orcid.org/0000-0001-9937-1087>

Martinius Th. van Genuchten  <https://orcid.org/0000-0003-1654-8858>

Paulo Couto  <https://orcid.org/0000-0002-3847-8638>

## REFERENCES

- Alves, R., Drexler, S., Silva, B., Silos, V., Toelke, J., & Siqueira, M. (2021). Elastic properties upscale for carbonate rocks using finite element numerical modeling and differential effective medium theory. In *First EAGE rock physics workshop in Latin America* (Vol. 1, pp. 1–5). European Association of Geoscientists & Engineers.
- Archilla, N. L., Missagia, R. M., Hollis, C., De Ceia, M. A. R., McDonald, S. A., Lima Neto, I. A., & Eastwood, D. S. (2016). Permeability and acoustic velocity controlling factors determined from X-ray tomography images of carbonate rocks. *AAPG Bulletin*, *100*(8), 1289–1309. <https://doi.org/10.1306/02251615044>
- Baychev, T. G., Jivkov, A. P., Rabbani, A., Raeini, A. Q., Xiong, Q., Lowe, T., & Withers, P. J. (2019). Reliability of algorithms interpreting topological and geometric properties of porous media for pore network modelling. *Transport in Porous Media*, *128*, 271–301. <https://doi.org/10.1007/s11242-019-01244-8>
- Blunt, M. J. (2017). *Multiphase flow in permeable media: A pore-scale perspective*. Cambridge University Press.
- Blunt, M. J., Bijeljic, B., Dong, H., Gharbi, O., Iglauer, S., Mostaghimi, P., Paluszny, A., & Pentland, C. (2013). Pore-scale imaging and modelling. *Advances in Water Resources*, *51*, 197–216. <https://doi.org/10.1016/j.advwatres.2012.03.003>
- Buades, A., Coll, B., & Morel, J. M. (2005). A non-local algorithm for image denoising. In *2005 IEEE computer society conference on computer vision and pattern recognition (CVPR'05)* (Vol. 2, pp. 60–65). IEEE.
- Bultreys, T., Boone, M. A., Boone, M. N., de Schryver, T., Maschaelle, B., van Hoorebeke, L., & Cnudde, V. (2015). Fast laboratory-based micro-computed tomography for pore-scale research: Illustrative experiments and perspectives on the future. *Advances in Water Resources*, *95*, 341–351. <https://doi.org/10.1016/j.advwatres.2015.05.012>
- Bultreys, T., De Boever, W., & Cnudde, V. (2016). Imaging and image-based fluid transport modeling at the pore scale geological materials: A practical introduction to the current state-of-the-art. *Earth-Science Reviews*, *155*, 93–128. <https://doi.org/10.1016/j.earscirev.2016.02.001>
- Carrillo, F. J., Soullaine, C., & Bourg, I. C. (2022). The impact of sub-resolution porosity on numerical simulations of multiphase flow. *Advances in Water Resources*, *161*, 104094. <https://doi.org/10.1016/j.advwatres.2021.104094>

- Corbett, P. W. M., & Borghi, L. F. (2013, 29–31). Lacustrine carbonates—For the purpose of reservoir characterisation are they different? In *2013 offshore technology conference Brasil, Rio de Janeiro—Brazil OTC Paper 24482*.
- Devarapalli, R. S., Islam, A., Faisal, T. F., Sassi, M., & Jouiad, M. (2017). Micro-CT and FIB–SEM imaging and pore structure characterization of dolomite rock at multiple scales. *Arabian Journal of Geosciences*, *10*, 1–12. <https://doi.org/10.1007/s12517-017-3120-z>
- De Vries, E. T., Raouf, A., & van Genuchten, M. Th. (2017). Multiscale modelling of dual-porosity media: A computational pore-scale study flow and solute transport. *Advances in Water Resources*, *105*, 82–95. <https://doi.org/10.1016/j.advwatres.2017.04.013>
- Drexler, S., Bastos Alves, R., Silos, V., Ferreira de Siqueira, M., & Toelke, J. (2022). New method to simulate digital petrophysical properties in heterogeneous carbonates using multiscale micro computed tomography imaging and customized laboratory experiments. In *International petroleum technology conference*. (pp. D012S124R003). IPTC.
- Dvorkin, J., Derzhi, N., Diaz, E., & Fang, Q. (2011). Relevance of computational rock physics. *Geophysics*, *76*(5), E141–E153. <https://doi.org/10.1190/geo2010-0352.1>
- Ferreira, M. E., Del Grande, M. R., Barros Ferreira, R. N., da Silva, A. F., da Silva, M. N. P., Tirapu-Azpiros, J., Lucas-Oliveira, E., Ferreira, A. G. A., Soares, R., Eckardt, C. B., Bonagamba, T. J., & Steiner, M. (2023). Full scale, microscopically resolved tomographies of sandstone and carbonate rocks augmented by experimental porosity and permeability values. *Scientific Data*, *10*, 368. <https://doi.org/10.1038/s41597-023-02259-z>
- Ferreira, T. R., Pires, L. F., Wildenschild, D., Brinatti, A. M., Borges, J. A. R., Auler, A. C., & dos Reis, A. M. H. (2019). Lime application effects on soil aggregate properties: Use of the mean weight diameter and synchrotron-based X-ray  $\mu$ CT techniques. *Geoderma*, *338*, 585–596. <https://doi.org/10.1016/j.geoderma.2018.10.035>
- Godoy, W. (2019). *Computational and experimental pore-scale studies of carbonate rock samples for the Brazilian pre-salt scenario* [Doctoral thesis, UFRJ/COPPE].
- Godoy, W., Pontedeiro, E. M., Hoerlle, F., Raouf, A., van Genuchten, M. T. H., Santiago, J., & Couto, P. (2019). Computational and experimental pore-scale studies of a carbonate rock sample. *Journal of Hydrology and Hydromechanics*, *67*(4), 372–383. <https://doi.org/10.2478/johh-2019-0009>
- Gostick, J., Aghighi, M., Hinebaugh, J., Tranter, T., Hoeh, M. A., Day, H., Spellacy, B., Sharqawy, M. H., Bazylak, A., Burns, A., Lehnert, W., & Putz, A. (2016). PenPNM: A pore network modeling package. *Computing in Science & Engineering*, *18*(4), 60–74.
- Hoerlle, F. O. L., Rios, E. H., Silva, W. G. A. L., Pontedeiro, E. M., Lima, M. C. O., Corbett, P. W. M., Alves, J. L., & Couto, P. (2018). Nuclear magnetic resonance to characterize the pore system of coquinas from Morro do Chaves Formation, Sergipe-Alagoas Basin, Brazil. *Brazilian Journal of Geophysics*, *36*(3), 1–8. <https://doi.org/10.22564/rbfg.v36i3.1960>
- Jiang, Z., van Dijke, M., Sorbie, K. S., & Couples, G. D. (2013). Representation of multiscale heterogeneity via multiscale pore networks. *Water Resources Research*, *49*(9), 5437–5449. <https://doi.org/10.1002/wrcr.20304>
- Kittler, J., & Illingworth, J. (1986). Minimum error thresholding. *Pattern Recognition*, *19*(1), 41–47. [https://doi.org/10.1016/0031-3203\(86\)90030-0](https://doi.org/10.1016/0031-3203(86)90030-0)
- Lima, M. C., Pontedeiro, E. M., Ramirez, M. G., Favoreto, J., Santos, H. N. D., van Genuchten, M. T., Borghi, L., Couto, P., & Raouf, A. (2022). Impacts of mineralogy on petrophysical properties. *Transport in Porous Media*, *145*(1), 103–125. <https://doi.org/10.1007/s11242-022-01829-w>
- Lucas, M., Vetterlein, D., Vogel, H.-J., & Schlüter, S. (2020). Revealing pore connectivity across scales and resolutions with X-ray CT. *European Journal of Soil Science*, *72*(2), 546–560. <https://doi.org/10.1111/ejss.12961>
- Luna, J. L., Perosi, F. A., Ribeiro, M. G. S., Souza, A., Boyd, A., Borghi, L. F., & Corbett, P. W. M. (2016). Petrophysical rock typing of coquinas from the Morro do Chaves Formation, Sergipe-Alagoas Basin (northeast Brazil). *Brazilian Journal of Geophysics*, *34*(4), 509–521. <https://doi.org/10.22564/rbfg.v34i4.883>
- Mazzullo, S. J. (2004). Overview of porosity in carbonate reservoirs. *Kansas Geological Society Bulletin*, *79*(1–2), 1–19.
- McClure, J. L., Li, J. E., Berrill, M., & Ramstad, T. (2021). The LBPM software package for simulating multiphase flow on digital images of porous rocks. *Computational Geosciences*, *25*, 871–895. <https://doi.org/10.1007/s10596-020-10028-9>
- Otsu, N. (1979). A threshold selection method from gray-level histograms. *IEEE Transactions on Systems, Man, and Cybernetics*, *9*, 62–66. <https://doi.org/10.1109/TSMC.1979.4310076>
- Pak, T., Archilha, N. L., Berg, S., & Butler, I. B. (2023). Design considerations for dynamic fluid flow in porous media experiments using X-ray computed micro tomography—A review. *Tomography of Materials and Structures*, *3*, 100017. <https://doi.org/10.1016/j.tmater.2023.100017>
- Raouf, A., Nick, H., Hassanizadeh, M., & Spiers, S. M. (2013). PoreFlow: A complex pore-network model for simulation of reactive transport in variably saturated porous media. *Computers & Geosciences*, *61*, 160–174.
- Ruspini, L. C., Øren, P. E., Berg, S., Masalmeh, S., Bultreys, T., Taberner, C., Sorop, T., Marcelis, F., Appel, M., Freeman, J., & Wilson, O. B. (2021). Multiscale digital rock analysis for complex rocks. *Transport in Porous Media*, *139*, 301–325. <https://doi.org/10.1007/s11242-021-01667-2>
- Saxena, N., Hofmann, R., Alpak, F. O., Berg, S., Dieterich, J., Agarwal, U., Tandon, K., Hunter, S., Freeman, J., & Wilson, O. B. (2017). References and benchmarks for pore-scale flow simulated using micro-ct images of porous media and digital rocks. *Advances in Water Resources*, *109*, 211–235. <https://doi.org/10.1016/j.advwatres.2017.09.007>
- Silveira, T. M., Hoerlle, F., Rocha, A. S., Lima, M. C., Ramirez, M. G., Pontedeiro, E. M., van Genuchten, M. T. H., Cruz, D. O., & Couto, P. (2022). Effects of carbonated water injection on the pore system of a carbonate rock (coquina). *Journal of Hydrology and Hydromechanics*, *70*(2), 257–268. <https://doi.org/10.2478/johh-2022-0001>
- Suhrer, M., Nie, X., Toelke, J., & Ma, S. (2020). Upscaling method for obtaining primary drainage capillary pressure and resistivity index with digital rock physics. In *International Petroleum Technology Conference*. (pp. D033S066R003). IPTC.
- Sullivan, S. P., Sederman, A. J., Johns, M. L., & Gladden, L. F. (2007). Verification of shear-thinning LB simulations in complex geometries. *Journal of Non-Newtonian Fluid Mechanics*, *143*, 59–63. <https://doi.org/10.1016/j.jnnfm.2006.12.008>

- Sun, H., Vega, S., & Tao, G. (2017). Analysis of heterogeneity and permeability anisotropy in carbonate rock samples using digital rock physics. *Journal of Petroleum Science and Engineering*, 156, 419–429. <https://doi.org/10.1016/j.petrol.2017.06.002>
- Vogel, H.-J., Tolke, J., Schulz, V., Krafczyk, M., & Roth, K. (2005). Comparison of a lattice-Boltzmann model, a full-morphology model, and a pore network model for determining capillary pressure—Saturation relationships. *Vadose Zone Journal*, 4(2), 380–388. <https://doi.org/10.2136/vzj2004.0114>

**How to cite this article:** Godoy, W., Pontedeiro, E. M., Barros, R. A. B. R., de Vries, E. T., Raoof, A., van Genuchten, M. T., & Couto, P. (2024). Modeling sub-resolution porosity of a heterogeneous carbonate rock sample. *Vadose Zone Journal*, e20348. <https://doi.org/10.1002/vzj2.20348>